nanomaterials

MDPI

Article

Microstructural Study of MgB_2 in the $LiBH_4$-MgH_2 Composite by Using TEM

Ou Jin [1,2], Yuanyuan Shang [3], Xiaohui Huang [2], Xiaoke Mu [2], Dorothée Vinga Szabó [1,2,4], Thi Thu Le [3], Stefan Wagner [1], Christian Kübel [2,4,5], Claudio Pistidda [3] and Astrid Pundt [1,*]

1 Institute of Applied Materials, Karlsruhe Institute of Technology, 76131 Karlsruhe, Germany; ou.jin@kit.edu (O.J.); dorothee.szabo@kit.edu (D.V.S.); stefan.wagner3@kit.edu (S.W.)
2 Institute of Nanotechnology, Karlsruhe Institute of Technology, 76344 Eggenstein-Leopoldshafen, Germany; xiaohui.huang@partner.kit.edu (X.H.); xiaoke.mu@kit.edu (X.M.); christian.kuebel@kit.edu (C.K.)
3 Institute of Hydrogen Technology, Helmholtz-Zentrum Hereon GmbH, 21502 Geesthacht, Germany; yuanyuan.shang@hzg.de (Y.S.); thi.le@hzg.de (T.T.L.); claudio.pistidda@hzg.de (C.P.)
4 Karlsruhe Nano Micro Facility, Karlsruhe Institute of Technology, 76344 Eggenstein-Leopoldshafen, Germany
5 Joint Research Laboratory Nanomaterials, Technical University of Darmstadt, 64206 Darmstadt, Germany
* Correspondence: astrid.pundt@kit.edu; Tel.: +49-721-608-42345

Abstract: The hampered kinetics of reactive hydride composites (RHCs) in hydrogen storage and release, which limits their use for extensive applications in hydrogen storage S1and energy conversion, can be improved using additives. However, the mechanism of the kinetic restriction and the additive effect on promoting the kinetics have remained unclear. These uncertainties are addressed by utilizing versatile transmission electron microscopy (TEM) on the $LiBH_4$-MgH_2 composite under the influence of the $3TiCl_3 \cdot AlCl_3$ additives. The formation of the MgB_2 phase, as the rate-limiting step, is emphatically studied. According to the observations, the heterogeneous nucleation of MgB_2 relies on different nucleation centers (Mg or TiB_2 and AlB_2). The varied nucleation and growth of MgB_2 are related to the in-plane strain energy density at the interface, resulting from the atomic misfit between MgB_2 and its nucleation centers. This leads to distinct MgB_2 morphologies (bars and platelets) and different performances in the dehydrogenation kinetics of $LiBH_4$-MgH_2. It was found that the formation of numerous MgB_2 platelets is regarded as the origin of the kinetic improvement. Therefore, to promote dehydrogenation kinetics in comparable RHC systems for hydrogen storage, it is suggested to select additives delivering a small atomic misfit.

Keywords: hydrogen storage; transmission electron microscopy; crystallography; reactive hydride composite; additive

Citation: Jin, O.; Shang, Y.; Huang, X.; Mu, X.; Szabó, D.V.; Le, T.T.; Wagner, S.; Kübel, C.; Pistidda, C.; Pundt, A. Microstructural Study of MgB_2 in the $LiBH_4$-MgH_2 Composite by Using TEM. *Nanomaterials* **2022**, *12*, 1893. https://doi.org/10.3390/nano12111893

Academic Editor: Cheol-Min Park

Received: 28 April 2022
Accepted: 30 May 2022
Published: 31 May 2022

1. Introduction

Hydrogen is a clean and reproducible energy carrier with the highest gravimetric energy density of ~120 kJ g^{-1}. For extensive applications of hydrogen, advanced hydrogen storage materials are demanded to store hydrogen safely and efficiently. Reactive hydride composites (RHCs) have been studied intensively due to their exceptionally reversible hydrogen storage capacity [1]. These materials were initially derived from light metal complex hydrides (e.g., $LiBH_4$, $LiNH_2$, $NaAlH_4$, etc.) in combination with a second hydride (e.g., LiH, MgH_2, etc.) [2–4]. Among various RHCs, the $LiBH_4$-MgH_2 composite is one of the most competitive candidates for both on- and off-board applications, based on the International Energy Agency Task 22 [5]. According to prior studies, the related decomposition reaction occurs in two steps [6]:

$$2LiBH_4 + MgH_2 \rightarrow 2LiBH_4 + Mg + H_2 \rightarrow 2LiH + MgB_2 + 4H_2 \quad (1)$$

Compared with the hydrogen capacity of ~18.5 wt% in pristine $LiBH_4$, about 11.4 wt% of hydrogen can still be yielded with the $LiBH_4$-MgH_2 composite, while the thermodynamic

properties are significantly improved by the addition of MgH_2, resulting in overall superior performance in hydrogen storage. For $LiBH_4$ alone, the standard enthalpy of decomposition is about 70 kJ mol^{-1} H_2 [7]. This value corresponds to a decomposition temperature of about 400 °C under atmospheric pressure [7–9]. For the $LiBH_4$-MgH_2 composite, the standard decomposition enthalpy is reduced to about 45 kJ mol^{-1} H_2 [9,10], which is ascribed to the exothermic formation of MgB_2 during the endothermic two-step decomposition process of the $LiBH_4$-MgH_2 composite (see Equation (1)) [3,10]. This results in a notable reduction in the decomposition temperature down to about 170 °C under atmospheric pressure [4,9].

However, in contrast to the thermodynamic predictions, the decomposition of the $LiBH_4$-MgH_2 composite for hydrogen release is kinetically limited and barely triggered at moderate temperatures [4,6]. Bösenberg et al. ascribed the sluggish kinetic behavior to the nucleation of MgB_2 as the rate-limiting step during dehydrogenation [11,12]. This is prominently reflected in the long incubation period, after the complete decomposition of MgH_2 into Mg (the first dehydrogenation step in Equation (1)) and before the massive decomposition of $LiBH_4$ (the second dehydrogenation step in Equation (1)).

Current research on enhancing the kinetics of hydride compounds mainly focuses on nanoconfinement using various carbon scaffolds and on utilizing transition metal-based additives [13–16]. The additives, in particular, provide an impressive boost to the dehydrogenation kinetics of RHCs, with their hydrogen storage capacities being well-preserved. As for the $LiBH_4$-MgH_2 composite, it has been reported that the enhanced kinetics can be attributed to a significant promotion of the heterogeneous nucleation of MgB_2 by additives [17,18]. However, their role in the decomposition path has not yet been explicitly understood due to a lack of microscopic investigations; thus, the mechanism of MgB_2 nucleation and growth in terms of crystallography has remained vague [11]. Complementing the missing knowledge is essential for understanding the reaction process behind the kinetic improvement of the material.

In this study, the additive effect on MgB_2 nucleation and growth in the $LiBH_4$-MgH_2 composite is clarified by determining the MgB_2 morphology and its crystallographic orientations toward nucleation centers. Transmission electron microscopy (TEM) studies were carried out on the microstructural evolution of MgB_2 in samples with and without Ti- and Al-based additives using a very high content. This allowed us to reveal the details of how the microstructural boundary conditions determine the decomposition kinetics of the system.

2. Experimental Section

2.1. Material Preparations

The reactants were provided in powder form by the following commercial suppliers: MgH_2 (95% purity) from Rockwood Lithium GmbH, $LiBH_4$ (95% purity) from Sigma-Aldrich, and $3TiCl_3 \cdot AlCl_3$ (about 76–78% purity) from Fischer Scientific. The $LiBH_4$-MgH_2 composite was prepared with a molar content of x% $3TiCl_3 \cdot AlCl_3$ (x = 0, 0.625, and 20). The large additive content of 20 mol% is chosen to maximize the additive effect on the MgB_2 morphology. To achieve a fine mixing of the reactants and an even dispersion of the additives, the prepared material mixtures (3 g)—namely, $2LiBH_4$-MgH_2 or $2LiBH_4$-MgH_2-$3TiCl_3 \cdot AlCl_3$—were charged into stainless-steel vials with stainless steel balls in a ball to powder ratio of 20:1. The milling proceeded for 400 min using a Spex 8000 M Mixer Mill. Both the powder handling and milling were always performed under an argon atmosphere in a glovebox (O_2, H_2O < 0.5 ppm).

2.2. Kinetic Measurements

The volumetric measurements were performed using a custom-built Sievert's-type apparatus. The milled sample (~170 mg) was charged into the stainless-steel sample holder of the measuring apparatus. The samples were annealed from room temperature to 400 °C at a heating rate of 10 °C min^{-1} under a hydrogen atmosphere of 4 bar. After reaching

the target temperature of 400 °C, the materials were kept under isothermal conditions for several hours.

2.3. XRD Experiments

The ex situ XRD experiments were based on a Bruker D8 Discover diffractometer equipped with a Cu X-ray source (λ = 1.54184 Å) and a 2D VANTEC detector. The operating voltage and current were 50 kV and 1000 mA. The diffraction patterns were acquired in the 2θ range from 10° to 90° with a step size of 0.005°, Δ2θ = 10°, and the exposure time for each step of 400 s. To prevent oxidation phenomena during the acquirement of the XRD pattern, the specimens were sealed in an argon-filled sample holder made of poly (methyl methacrylate) (PMMA).

2.4. TEM Experiments

TEM experiments were performed using a Themis-Z 60-300 (Thermo Fisher Scientific Inc., Waltham, MA, USA) equipped with a monochromator and double aberration correctors (probe and image Cs correctors), operated at 300 kV. TEM sample preparation was carried out under an argon atmosphere in a glovebox (O_2, H_2O < 0.5 ppm). Sample powders were dispersed in toluene and ultra-sonicated for 1 min before being distributed on lacey-carbon coated gold TEM grids S166-A3-V (Ted Pella Inc., Redding, CA, USA). Subsequently, they were transferred under argon from the glovebox into the microscope with a vacuum transfer holder 648 (Gatan Inc., Pleasanton, CA, USA).

The beam current varied from 50 to 100 pA throughout all TEM experiments. Selected area electron diffraction (SAED) patterns, TEM, and high-resolution TEM (HRTEM) images were collected using a OneView camera (Gatan Inc., Pleasanton, CA, USA). Scanning TEM (STEM) images were recorded via a high-angle annular dark-field (HAADF) detector with a convergence angle of 21.5 mrad and a camera length of 93 mm. Energy-dispersive X-ray spectroscopy (EDX) spectrum-imaging (SI) was executed with a Super-X windowless EDX detector (Thermo Fisher Scientific Inc., Waltham, MA, USA) using the same parameters as in STEM mode.

Electron tomography was carried out using a Fischione 2020 tomography holder in STEM mode with the same STEM parameters as mentioned above. HAADF-STEM Tilt series with image dimensions of 2048 × 2048 pixels were collected using Xplore3D (Thermo Fisher Scientific) over a tilt range in increments of 2° from −72° to 78° for the desorbed $2LiBH_4$-MgH_2 without additives and from −72° to 68° for the desorbed $2LiBH_4$-MgH_2 with 20 mol% $3TiCl_3 \cdot AlCl_3$. The alignment of the tilt series was performed by IMOD using 10 nm gold colloidal particles as fiducial markers, which leads to the respective mean residual error of 0.736 and 0.129 voxels [19]. The aligned tilt series were then reconstructed using the algorithm simultaneous iterative reconstruction technique (SIRT) with 100 iterations by Inspect3D (Thermo Fisher Scientific) [20]. The 3D visualizations were realized by Avizo 2020.2 (Thermo Fisher Scientific).

In addition, 4D-STEM measurements were carried out in μ probe mode using the OneView camera, with a convergence angle of 0.47 mrad, a camera length of 580 mm, and an acquisition time of 60 ms for each diffraction pattern, and a dose of ~1.5×10^5 e nm^{-2}. STEM electron energy-loss spectroscopy (EELS) SI was acquired using a Gatan Continuum 970 HighRes imaging filter (GIF) (Gatan Inc., Pleasanton, CA, USA) in dual-EELS mode with 5 ms acquisition time for each low-loss spectrum, 20 ms for each high-loss spectrum, 21.5 mrad convergence angle, 40 mrad collection angle, and 0.3 eV per channel energy dispersion, leading to a measured energy spread of 2.0 eV on the camera. Both the EDX SI and EELS SI data were denoised via principal component analysis (PCA), which effectively reduces the random noise generated during the signal recording [21,22].

3. Results and Discussion

3.1. Material Characterization via XRD and Kinetic Performance

Figure 1a shows the X-ray diffraction (XRD) results of the system $2LiBH_4$-MgH_2 with x mol% $3TiCl_3 \cdot AlCl_3$ (x = 0, 0.625, and 20) in two different states: as-milled and after desorption. In general, no significant variation is visible for the sample without additives and the one containing 0.625 mol% $3TiCl_3 \cdot AlCl_3$. However, after increasing the additive content to a high value of 20 mol%, the $LiBH_4$ peaks for the as-milled state and the MgB_2 peaks for the after-desorption state noticeably weakened, whereas strong LiCl peaks appeared for both states. This difference can be attributed to the reaction between $LiBH_4$ and $3TiCl_3 \cdot AlCl_3$, which consumed a significant amount of $LiBH_4$ that is responsible for the generation of MgB_2 [18].

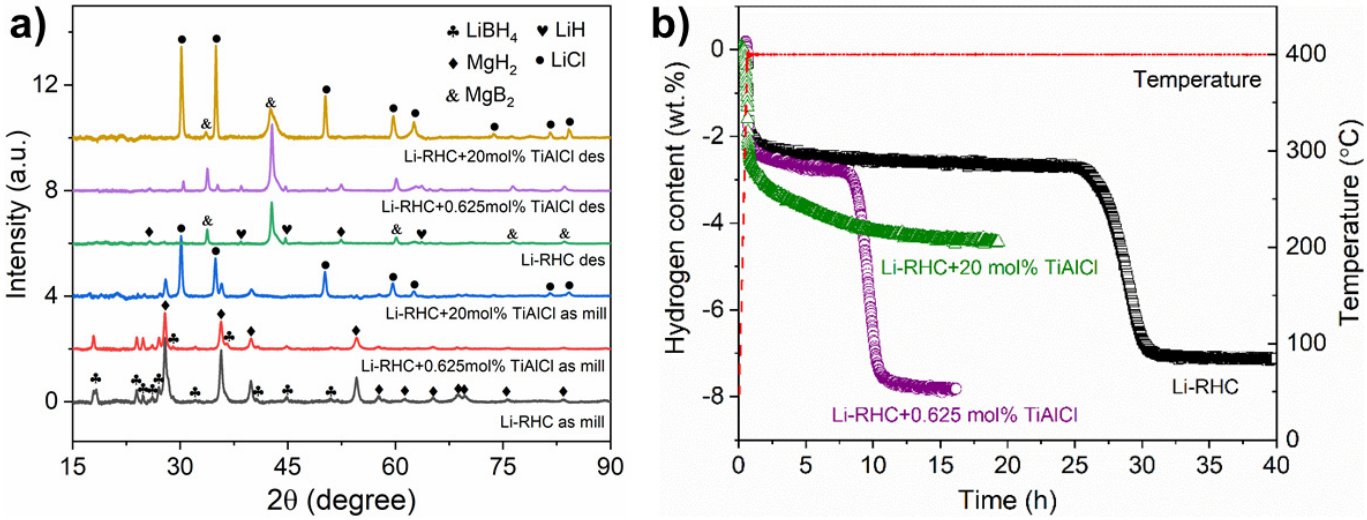

Figure 1. (**a**) XRD patterns of $2LiBH_4$-MgH_2 with x mol% $3TiCl_3 \cdot AlCl_3$ (x = 0, 0.625, and 20) after milling and after desorption; (**b**) desorption kinetics of $2LiBH_4$-MgH_2 with x mol% $3TiCl_3 \cdot AlCl_3$ (x = 0, 0.625, and 20) at 400 °C and under 4 bar H_2.

The kinetic performance of the corresponding materials is visualized in Figure 1b. In comparison with the pristine material, the incubation period was reduced from ~25 h to ~8 h with an additive content of 0.625 mol%. By adding 20 mol% $3TiCl_3 \cdot AlCl_3$, the incubation stage disappeared, and the kinetics of the second desorption step for hydrogen release changed. The reduced hydrogen storage capacity of ~5 wt% for the 20 mol% $3TiCl_3 \cdot AlCl_3$ sample is due to the significant consumption of $LiBH_4$ during the reaction with additives.

3.2. MgB_2 Formation without the Influence of Additives

Figure 2a presents the morphology of the decomposed $LiBH_4$-MgH_2 composite—namely, LiH and MgB_2. The local electron diffraction pattern indicates the existence of MgB_2 crystals with a hexagonal closed packed (hcp) structure (P6m/mm, No. 191). The absence of crystallographic information on LiH is likely due to its instability under electron illumination and the low scattering power of Li and H. One impressive feature in Figure 2a is the bar-like morphology of crystals with a parallel arrangement. They were identified as MgB_2 by HRTEM (Figure 2b), its fast Fourier transform (FFT) pattern, and the EDXS elemental map of Mg acquired from the corresponding area in Figure 2a (see Figure S1). The primary growth direction of MgB_2 bars is thus determined to be $[1\bar{2}10]_{MgB_2}$, which is along the long axis of a MgB_2 bar (the inset in Figure 2b).

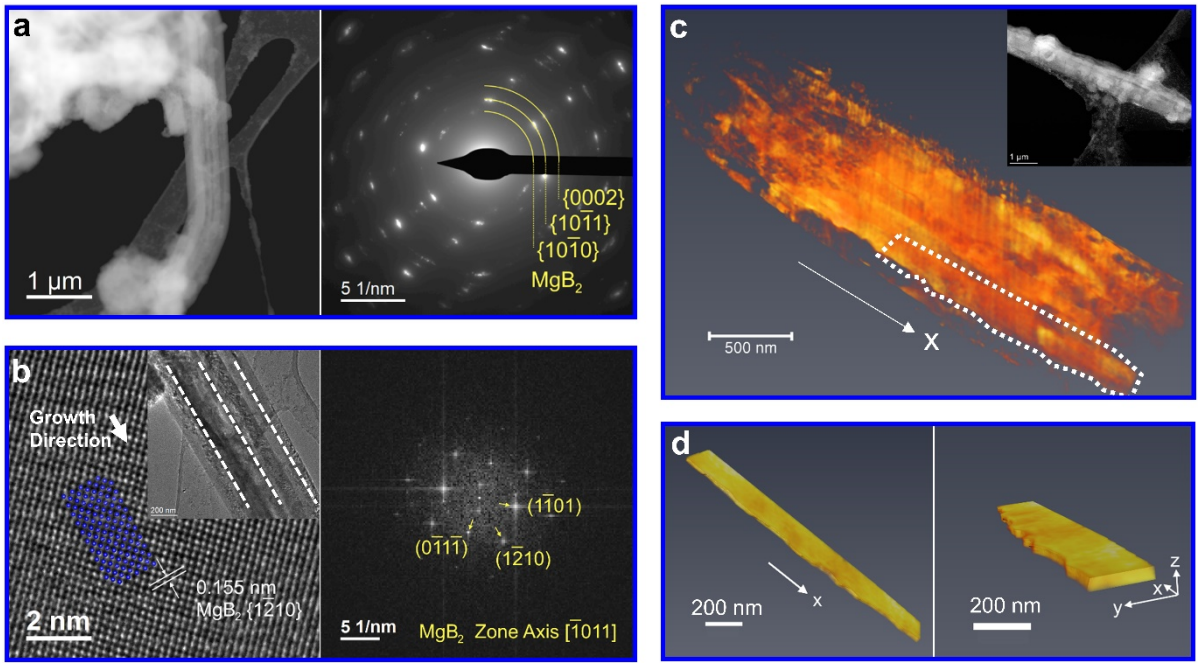

Figure 2. The results of 2LiBH$_4$-MgH$_2$ without additives after desorption: (**a**) STEM-HAADF image and the corresponding electron diffraction pattern; (**b**) HRTEM image with an inset of the local zoomed-out overview showing the growth direction of MgB_2 bars, and the corresponding FFT; (**c**) volume rendering from tomographic reconstruction of MgB_2 bars with an inset showing the corresponding STEM-HAADF image; (**d**) volume rendering of one selected MgB_2 bar chosen from (**c**).

For a more comprehensive understanding of the MgB_2 morphology, electron tomography was conducted. Figure 2c shows a volume rendering of MgB_2 bars, reconstructed from the STEM-HAADF tomographic data, and Figure 2d exhibits a single MgB_2 bar extracted from the selected region in Figure 2c. It should be noted that MgB_2 bars possess a rectangular shape. This can be understood in combination with the study by Lee et al., claiming that a growth constraint exists for MgB_2 along the c-axis $[0002]_{MgB_2}$ [23], which is consistent with our investigation, as the constrained direction $[0002]_{MgB_2}$ (z-axis in Figure 2d) lays perpendicular to the observed growth direction $[1\bar{2}10]_{MgB_2}$ (x-axis). Given the rectangular MgB_2 bars, another growing direction along the y-axis corresponds to $[10\bar{1}0]_{MgB_2}$, along which the growth is also limited to some extent. This is discussed in Section 3.5.

The observation of parallel MgB_2 bars in Figure 2a implies that their nucleation and growth initially proceeded from the same class of atomic layers of one crystalline nucleation center. Given the two-step decomposition of the LiBH$_4$-MgH$_2$ composite (Equation (1)), Mg and LiBH$_4$ are candidates for this nucleation center. Since LiBH$_4$ has a melting point of approximately 275 °C and, therefore, remains in the liquid state during the desorption at 400 °C, Mg has to be the nucleation center for the heterogeneous nucleation of these MgB_2 bars. Another requirement for the nucleation center is that it has to provide a sufficiently large superficial plane to nucleate several MgB_2 bars with a lateral size of about 200 nm (Figure 2d). The observed Mg grains are large enough, with a size up to about 1 µm to meet this requirement (see Figure S2).

3.3. MgB_2 Formation under the Influence of Additives

To reveal the additive's effect on MgB_2 nucleation and growth, an overdose of 20 mol% 3TiCl$_3$·AlCl$_3$ was taken for the LiBH$_4$-MgH$_2$ composite. Figure 3a shows the material morphology after desorption. According to the XRD result (Figure 1a) and the local electron diffraction pattern (Figure 3a), the element Mg exists only as MgB_2. Therefore, the Mg EDX map (Figure 3b) can be directly regarded as representing the distribution of MgB_2,

which is comparable with the bright contrast in the HAADF image (Figure 3b). In general, the MgB_2 morphology changed significantly, compared with what was previously reported in Section 3.2.

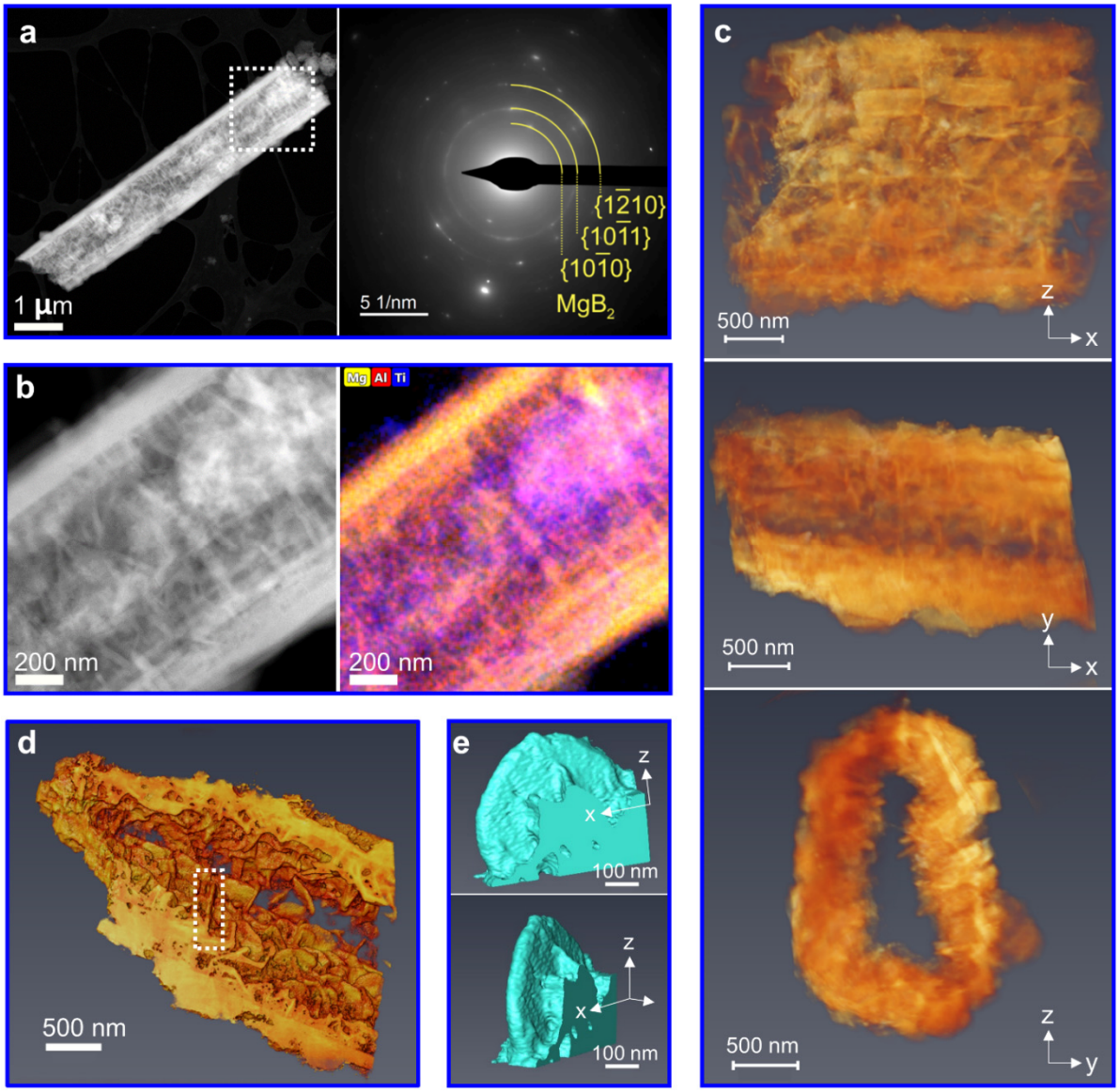

Figure 3. The results of $2LiBH_4$-MgH_2 with 20 mol% $3TiCl_3 \cdot AlCl_3$ after desorption: (**a**) STEM-HAADF image and the corresponding electron diffraction pattern; (**b**) STEM-HAADF image of the selected area in (**a**) and EDXS elemental map of Mg (yellow), Ti (blue), and Al (red); (**c**) volume rendering from tomographic reconstruction of a MgB_2 hollow tube viewed at different angles; (**d**) surface rendering of the cross-section of (**c**); (**e**) surface rendering of a segmented MgB_2 platelet selected from (**d**).

Figure 3c exhibits a reconstructed volume rendering of MgB_2 in different directions. In this case, two different MgB_2 morphologies can be distinguished. Orienting along the x-axis, the parallel-lying MgB_2 bars grow into a hollow tube. Inside the tube, the second morphology of platelet-like MgB_2 can be identified. It can be seen in Figure 3d that these MgB_2 platelets grow from the tube walls of MgB_2 bars in a more or less random orientation. For a closer look at these MgB_2 platelets, one piece was cut out from Figure 3d and displayed as a segmented surface rendering in Figure 3e. In contrast to the rectangular shape of the MgB_2 bars, these MgB_2 platelets with a lateral size of about 500 nm possess a more irregular or semi-circular shape. In other words, no primary growth direction is

observed for the MgB_2 platelets. In addition, the MgB_2 morphology of the sample with 0.625 mol% $3TiCl_3 \cdot AlCl_3$ can be found in Figure S3 for comparison.

The platelet-like MgB_2 morphology hints at another nucleation center that facilitates the formation of the MgB_2 platelets. We suggest that this nucleation center stems from the additives, so the identification and location of these additives is another point of interest. As reported by T.-T. Le et al., the additive $3TiCl_3 \cdot AlCl_3$ can react with $LiBH_4$ and generate either $AlTi_3$ or TiB_2 and AlB_2 [18]. Accordingly, rather than the initial additive $3TiCl_3 \cdot AlCl_3$, these reaction products are considered to be the heterogeneous nucleation centers for the MgB_2 platelets. Based on the STEM-EDX map in Figure 3b, both Ti and Al are dispersed inside the MgB_2 tube, which is also indicative of their role as the nucleation center (also see Figure S4).

For further studies, the EELS SI was acquired. Figure 4a displays the summed elemental map based on the EEL spectrum in Figure 4b, comprising B K-edge in red, Ti $L_{2,3}$-edge in blue, and Mg K-edge in yellow (Figure 4c). Therefore, the orange platelets that result from an overlap between Mg (yellow) and B (red) indicate the elemental correlation between Mg and B and suggest the location of MgB_2. Furthermore, the background-subtracted B K-edge recorded in the orange area exhibits a pre-peak at about 190 eV (Figure 4b). This fine structure is evidence of a high and unfilled p-like density of states of Boron, which indicates the bonding between Mg and B and verifies the existence of MgB_2 [24].

Similarly, the purple agglomerates in Figure 4a represent the spatial elemental correlation between Ti (blue) and B (red), which disperse around the orange MgB_2 platelets. According to the HRTEM image and its FFT pattern (Figure 4d), the presence of TiB_2 rather than $AlTi_3$ can be confirmed already after the ball milling process. The HRTEM image corresponding to the purple agglomerates in Figure 4a can be found in Figure S5, which shows a further growth of TiB_2 particles up to ~20 nm after desorption likely due to Ostwald ripening. The beneficial effect of TiB_2 on accelerating the decomposition of the $LiBH_4$-MgH_2 composite was already reported by some studies, which also supports our characterizations [25,26]. Since AlB_2 and TiB_2 have the same space group (P6m/mm, No. 191), with almost the same lattice constants, AlB_2 might have the same effect as TiB_2, although they cannot be distinguished here.

In Figure 5, the relationship between the crystallography and the morphology of the MgB_2 bars and MgB_2 platelets is revealed via 4D-STEM. Figure 5b–e provide local electron-diffraction patterns acquired from areas B-E in Figure 5a. A fragment of the MgB_2 bar with a rectangular shape can be found in area B of Figure 5a, with the short axis along $[10\bar{1}0]_{MgB_2}$ (Figure 5b). Figure 5d,e indicate the long axis direction of the MgB_2 bars being along $[1\bar{2}10]_{MgB_2}$. These investigated orientations are consistent with Figure 2. Thus, it can be summarized that the morphology of MgB_2 bars with a rectangular shape has the long axis direction oriented along $[1\bar{2}10]_{MgB_2}$, the short axis direction along $[10\bar{1}0]_{MgB_2}$, and the thin direction along $[0002]_{MgB_2}$. For MgB_2 platelets, the thin direction of a platelet, which is also regarded as the growth-restricted direction, is along $[0002]_{MgB_2}$ (Figure 5a,c). This growth restriction observed for more other MgB_2 platelets can be seen in Figure S6.

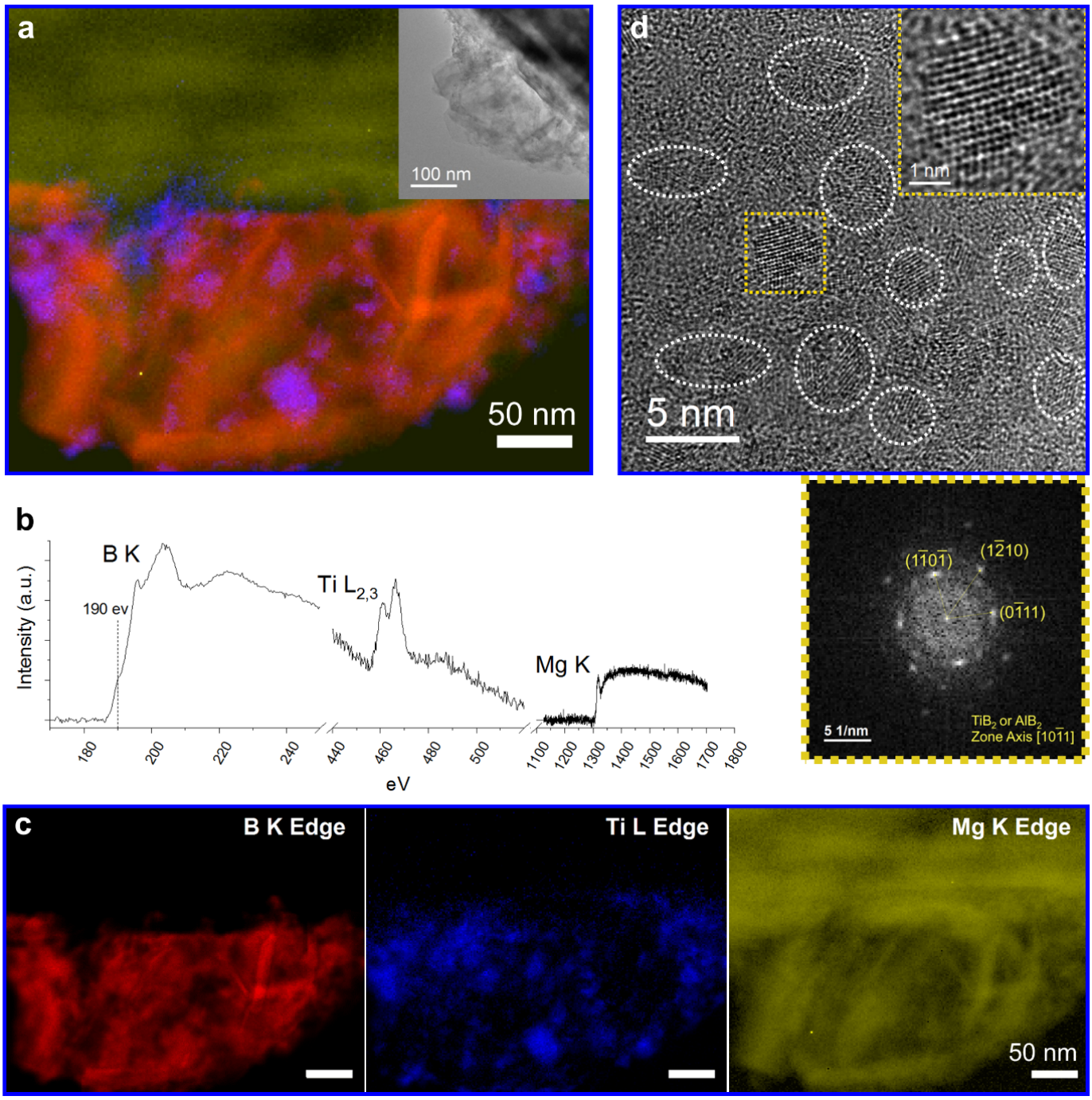

Figure 4. The results of $2LiBH_4$-MgH_2 with 20 mol% $3TiCl_3 \cdot AlCl_3$: (**a**) summed EELS elemental map, based on the background-subtracted EEL spectrum (**b**), and comprising the elemental distribution of B K-edge (red), Ti $L_{2,3}$-edge (blue), and Mg K-edge (yellow) (**c**). The inset of a TEM bright-field image was recorded in the same area. In (**a**), the orange color is coming from the overlap between yellow and red, and is thus indicative of the correlation between Mg and B. Similarly, the color purple stands for the correlation between Ti and B. (**d**) HRTEM image of TiB_2 (and AlB_2) nanoparticles just after milling and the corresponding FFT of the inset showing the lattice of a single-crystalline TiB_2 particle.

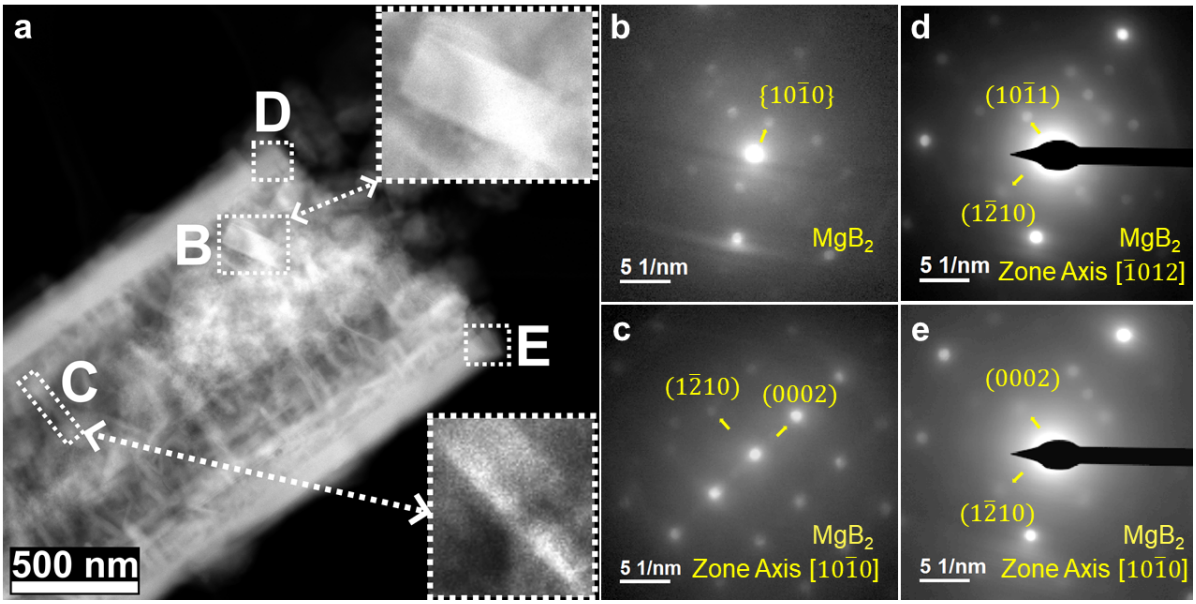

Figure 5. The results of $2LiBH_4$-MgH_2 with 20 mol% $3TiCl_3 \cdot AlCl_3$ after desorption: (**a**) STEM-HAADF image with insets of magnified areas B and C; (**b**–**e**) diffraction patterns acquired in the corresponding areas B–E in (**a**), which show the crystallographic orientation of MgB_2 bars and platelets.

3.4. Analysis of Orientation Relationships

Given the small size of TiB_2 or/and AlB_2 nanoparticles only up to about 20 nm (Figure S5) and the complexity of the overlapping phases, the interface between the nucleation centers and MgB_2 cannot be investigated in the experiment. For this reason, their orientation relationships (ORs) cannot be experimentally determined in a conventional way by focusing on the interface. To determine the orientation relationship between the different nucleation centers and MgB_2, we took advantage of the edge-to-edge matching model [27–31].

The edge-to-edge matching model builds on minimizing the energy of coherent interfaces between two adjacent materials, in this case, the nucleation center and the nucleating particle [27,30]. According to this model, the heterogeneous nucleation between the two phases is controlled by their interatomic misfit and their interplanar mismatch. The interatomic misfit is determined along the matching directions of the two phases. These matching directions are selected among their close or nearly close-packed directions identified by the linear atomic density. The interplanar mismatch (d-value mismatch) is determined between the matching planes, which are chosen from the close or nearly close-packed planes. As a rule of thumb, the interatomic misfit and the interplanar mismatch should generally not exceed 10% and 6%, which are regarded as the critical values [27]. On the other hand, minimizing the interatomic misfit has a higher priority than the d-value mismatch from an energetic perspective. A slight excess of the d-value mismatch above 6% is still acceptable, which can be subsequently refined by an additional rotation between the two phases about their matching directions [30].

Since MgB_2, Mg, and TiB_2 (and AlB_2) have a similar hexagonal close-packed (hcp) crystal structure, their close or nearly close-packed directions and planes are similarly indexed. Based on their crystallographic characteristics, there are four possible close-packed directions $\langle 10\bar{1}0 \rangle$, $\langle 0002 \rangle$, $\langle 1\bar{2}10 \rangle$, and $\langle 1\bar{1}23 \rangle$ and four possible close-packed planes $\{10\bar{1}0\}$, $\{10\bar{1}1\}$, $\{0002\}$, and $\{1\bar{2}10\}$ [29]. According to our observations, two distinct MgB_2 morphologies were introduced:

1. Rectangular-shaped MgB_2 bars that are constrained along $[0002]_{MgB_2}$ and $[10\bar{1}0]_{MgB_2}$, and primarily grow along $[1\bar{2}10]_{MgB_2}$ from Mg grains (Figures 2 and 5);

2. Semi-circular shaped MgB_2 platelets that are constrained along $[0002]_{MgB_2}$ and grow from TiB_2 (and AlB_2) nanoparticles (Figures 3–5).

Given the large interatomic misfit of $\langle 0002 \rangle_{MgB_2}$, compared with the close-packed directions of Mg and TiB_2 (and AlB_2) (see Tables S1 and S2), $\{0002\}_{MgB_2}$, as one of the close-packed planes, is supposed to be the matching plane for the heterogeneous nucleation of both MgB_2 bars and MgB_2 platelets on Mg and TiB_2 (and AlB_2).

For the MgB_2 bars, the interplanar mismatch of $\{0002\}_{MgB_2}$ concerning the possible matching plane of Mg is listed in Table 1. The only suitable matching planes with a reasonably low interplanar mismatch of ~8.5% are $\{0002\}_{MgB_2} \mid \{1\bar{2}10\}_{Mg}$. In addition, since the matching $\{0002\}_{MgB_2}$ the plane should include the matching direction, only $\langle 10\bar{1}0 \rangle_{MgB_2}$ and $\langle 1\bar{2}10 \rangle_{MgB_2}$ fit for the matching direction. Similarly, only $\langle 10\bar{1}0 \rangle_{Mg}$ and $\langle 0002 \rangle_{Mg}$ are fitting for Mg, with $\{1\bar{2}10\}_{Mg}$ being the matching plane. The resulting pairs of the matching directions with an interatomic misfit smaller than 10% turn out to be $\langle 10\bar{1}0 \rangle_{MgB_2} \,||\, \langle 10\bar{1}0 \rangle_{Mg}$ and $\langle 10\bar{1}0 \rangle_{MgB_2} \,||\, \langle 0002 \rangle_{Mg}$ (Table 2). For a refined matching, a tilting angle between $\{0002\}_{MgB_2}$ and $\{1\bar{2}10\}_{Mg}$ should also be considered (see Figure S7a,b). In summary, the possible orientation relationships between MgB_2 and Mg are predicted to be as follows:

$$\langle 10\bar{1}0 \rangle_{MgB_2} \,||\, \langle 10\bar{1}0 \rangle_{Mg} \quad \{0002\}_{MgB_2} \sim 2.0^\circ \; from \; \{1\bar{2}10\}_{Mg}$$
$$\langle 10\bar{1}0 \rangle_{MgB_2} \,||\, \langle 0002 \rangle_{Mg} \quad \{0002\}_{MgB_2} \text{</mo>} \; from \; \{1\bar{2}10\}_{Mg}$$

Table 1. The interplanar misfit between MgB_2 {0002} and possible match planes of Mg nucleation center (%).

MgB_2/Mg	**$\{0002\} \mid \{10\bar{1}1\}$**	**$\{0002\} \mid \{0002\}$**	**$\{0002\} \mid \{10\bar{1}0\}$**	**$\{0002\} \mid \{1\bar{2}10\}$**
	39.8	48.6	58.4	8.5

Table 2. The interatomic misfit along possible matching directions between MgB_2 and Mg nucleation center (%).

MgB_2/Mg	**$\langle 10\bar{1}0 \rangle \,||\, \langle 10\bar{1}0 \rangle$**	**$\langle 10\bar{1}0 \rangle \,||\, \langle 0002 \rangle$**	**$\langle 1\bar{2}10 \rangle \,||\, \langle 10\bar{1}0 \rangle$**	**$\langle 1\bar{2}10 \rangle \,||\, \langle 0002 \rangle$**
	−4.2	2.1	−80.8	−69.5

The orientation relationships between MgB_2 and TiB_2 (and/or AlB_2) can be derived in the same way. The related interplanar mismatch is given in Table 3. In this case, it appears that $\{0002\}_{MgB_2}$ pairing with $\{0002\}_{TiB_2}$ (and/or $\{0002\}_{AlB_2}$) results in the least mismatch.

Table 3. The interplanar misfit between MgB_2 {0002} and possible match planes of MB_2 (M = Ti or Al) nucleation center (%).

MgB_2/MB_2	**$\{0002\} \mid \{10\bar{1}1\}$**	**$\{0002\} \mid \{0002\}$**	**$\{0002\} \mid \{10\bar{1}0\}$**	**$\{0002\} \mid \{1\bar{2}10\}$**
TiB_2	−15.8	8.2	−49.2	13.9
AlB_2	−15.5	7.6	−47.9	14.6

According to Table 4, the possible matching direction are $\langle 10\bar{1}0 \rangle$ and $\langle 1\bar{2}10 \rangle$ for both MgB_2 and TiB_2 (and/or AlB_2). The least interatomic misfit is thus obtained for the matching directions $\langle 10\bar{1}0 \rangle_{MgB_2} \,||\, \langle 10\bar{1}0 \rangle_{TiB_2\ (AlB_2)}$ and $\langle 1\bar{2}10 \rangle_{MgB_2} \,||\, \langle 1\bar{2}10 \rangle_{TiB_2\ (AlB_2)}$. Considering

the rotation between the two matching planes (see Figure S7c,d), the possible orientation relationships between MgB_2 and TiB_2 (and/or AlB_2) are as follows:

$$\langle 10\bar{1}0\rangle_{MgB_2} \,||\, \langle 10\bar{1}0\rangle_{TiB_2\ (AlB_2)} \quad \{0002\}_{MgB_2} \sim 0.03^\circ \ from \ \{0002\}_{TiB_2\ (AlB_2)}$$
$$\langle 1\bar{2}10\rangle_{MgB_2} \,||\, \langle 1\bar{2}10\rangle_{TiB_2\ (AlB_2)} \quad \{0002\}_{MgB_2} \sim 0.01^\circ \ from \ \{0002\}_{TiB_2\ (AlB_2)}$$

Table 4. The interatomic misfit along possible matching directions between MgB_2 and MB_2 (M = Ti or Al) nucleation center (%).

MgB_2/MB_2	$\langle 1\bar{2}10\rangle \,||\, \langle 1\bar{2}10\rangle$	$\langle 1\bar{2}10\rangle \,||\, \langle 10\bar{1}0\rangle$	$\langle 10\bar{1}0\rangle \,||\, \langle 1\bar{2}10\rangle$	$\langle 10\bar{1}0\rangle \,||\, \langle 10\bar{1}0\rangle$
TiB_2	1.7	−70.3	43.3	1.7
AlB_2	2.6	−68.7	43.8	2.6

3.5. Varied Morphology and Kinetics

As predicted, the heterogeneous nucleation of MgB_2 on Mg grains occurs along the directions $[10\bar{1}0]_{MgB_2}$ and $[0002]_{MgB_2}$. It is noted that the predicted orientation of MgB_2 agrees with our experimental observations on the morphology of the MgB_2 bars, as demonstrated in Figures 2 and 5. The subsequent growth dominantly along $[1\bar{2}10]_{MgB_2}$ is likely due to the constrained growth along $[0002]_{MgB_2}$ as well as $[10\bar{1}0]_{MgB_2}$, both of which are in-plane directions at the MgB_2/Mg interface, resulting in a rectangular-shaped MgB_2 bar. Conversely, the growth of the MgB_2 platelets on TiB_2 nanoparticles is only limited along $[0002]_{MgB_2}$, one of the in-plane directions at the MgB_2/TiB_2 interface. According to Figure 3, these MgB_2 platelets with a semi-circular shape are likely growing more randomly without a preferred growth direction.

The different MgB_2 morphologies, ranging from MgB_2 bars to MgB_2 platelets, are here ascribed to the different extent of the strain energy density induced at the interface to the nucleation center. Different aspect ratios of $[1\bar{2}10] : [10\bar{1}0] : [0002]$ are determined to be about 50:5:1 for MgB_2 bars growing on Mg (Figure 2d), and about 15:15:1 for MgB_2 platelets growing on TiB_2 (Figure 3e). As the elastic-strain energy density ϵ is proportional to $Y\varepsilon^2$, where Y is Young's modulus of MgB_2, and ε is the atomic misfit between MgB_2 and Mg or TiB_2, the strain energy density can be thus roughly estimated by the related misfits, by assuming constant Y for simplicity. Along the interatomic direction $[10\bar{1}0]_{MgB_2}$, the induced strain energy density is approximated to be more than 6 times larger for MgB_2 on Mg grains (misfit of 4.2%) than for MgB_2 on TiB_2 nanoparticles (misfit of 1.7%), as listed in Tables 2 and 4. Thus, the MgB_2 growth is hindered along the direction $[10\bar{1}0]_{MgB_2}$ on Mg, leading to a lower aspect ratio $[10\bar{1}0] : [0002]$ of 5:1 for MgB_2 growth on Mg, compared with 15:1 for MgB_2 growth on TiB_2. The compelling growth restriction along [0002] can be also well-interpreted by the large interplanar misfit up to ~8% in both cases (Tables 1 and 3). Therefore, the difference in the elastic strain energy density here is considered to be the root of the different MgB_2 morphologies, and furthermore, the changed desorption kinetic performances.

Figure 6 illustrates the complete process of the MgB_2 formation as discussed above. For MgB_2 growing on Mg grains, the further growth along $[10\bar{1}0]_{MgB_2}$ is hampered due to a huge in-plane strain energy density, which forces itself to mainly grow in the out-of-plane direction $[1\bar{2}10]_{MgB_2}$, ending up with these parallel-lying rectangular MgB_2 bars (Figure 6a). On the contrary, with an interatomic misfit of 1.7% between MgB_2 and TiB_2 along $[10\bar{1}0]_{MgB_2}$, this in-plane growth constraint is not relevant (Figure 6b). The further growth of MgB_2 along the in-plane direction $[10\bar{1}0]_{MgB_2}$, and the out-of-plane direction $[1\bar{2}10]_{MgB_2}$ can thus continuously proceed, leading to semi-circular shaped MgB_2 platelets. Furthermore, a critical value of the interatomic misfit between 1.7% and 4.2% may be

expected, above which the in-plane growth of MgB_2 is restricted. This may result in a deceleration of the MgB_2 nucleation and growth and, therefore, a decelerated desorption kinetics for the $LiBH_4$-MgH_2 composite.

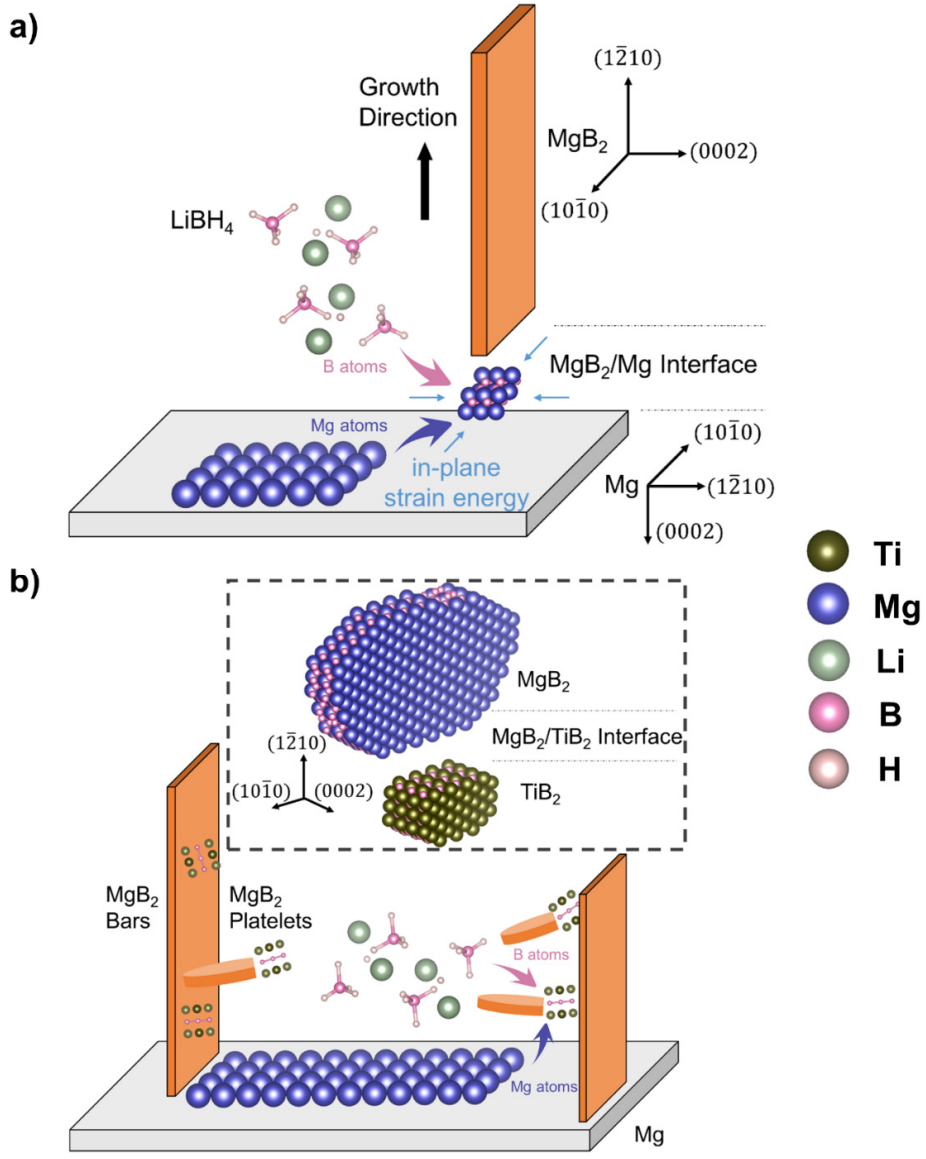

Figure 6. (**a**) Schematic illustration of how MgB_2 bars are generated based on Mg grains following a certain crystallographic orientation relationship. The nucleation and growth of MgB_2 may occur at the MgB_2/Mg interface under control of the in-plane strain energy density; (**b**) schematic illustration of the nucleation and growth of MgB_2 platelets based on TiB_2 nanoparticles at the MgB_2/TiB_2 interface.

As the growth of MgB_2 commonly leads to hexagonal plates [23], we speculate that the MgB_2 formation occurs at the interface between MgB_2 and its nucleation centers rather than on the MgB_2 surface exposed to the liquefied $LiBH_4$. This means that the formation of MgB_2 is always under the control of the in-plane strain energy density (Figure 6). From this perspective, the highly regular rectangular shape of the MgB_2 bars can be explained consistently. However, future in situ experiments are still required to confirm this speculation.

4. Conclusions

Manifold TEM studies on the $LiBH_4$-MgH_2 composite with and without additives, combined with the predictions of the edge-to-edge matching model on the orientation relationship between the nucleation center and the resulting MgB_2 phase, contribute to a better understanding of the RHCs' kinetics. According to this, the additives deliver a large number of nucleation centers with a small interatomic misfit of 1.7% to MgB_2, corresponding to low in-plane strain energy density. They facilitate the nucleation and growth of MgB_2, leading to the morphology of MgB_2 semi-circular platelets. In contrast, large in-plane strain energy density is expected for the formation of MgB_2 bars on Mg, limiting the growth of MgB_2 and consequently slowing down the dehydrogenation kinetics. To further improve the kinetic performance of the $LiBH_4$-MgH_2 composite, we suggest that the atomic misfit delivered by additives with respect to MgB_2 should be considered for future additive selection. It is also believed that these conclusions hold for other RHC systems interesting for hydrogen energy storage and release.

Supplementary Materials: The supporting information can be downloaded at: https://www.mdpi.com/article/10.3390/nano12111893/s1, Figure S1: The results of $2LiBH_4$-MgH_2 without additives after desorption: STEM-HAADF image acquired from the corresponding position in Figure 2a and EDX elemental map of Mg; Figure S2: The results of $2LiBH_4$-MgH_2 with 5 wt% $3TiCl_3{\cdot}AlCl_3$ after incomplete desorption: (a) STEM-HAADF image, and (b) the corresponding electron diffraction pattern; (c) STEM-HAADF image acquired from the selected area in (a) and (d) the corresponding EDX elemental map of Mg; Figure S3: The results of $2LiBH_4$-MgH_2 with 0.625 mol% $3TiCl_3{\cdot}AlCl_3$ after desorption: (a) STEM-HAADF images showing the morphology of the generated MgB_2 crystals; (b) electron diffraction pattern; (c) STEM-HAADF image acquired from the corresponding position in (a), and EDX map of Mg; Figure S4: The results of $2LiBH_4$-MgH_2 with 20 mol% $3TiCl_3{\cdot}AlCl_3$ after desorption: STEM-HAADF image acquired from the selected position in Figure 3a, and the corresponding EDX elemental map of Mg, Ti, and Al; Figure S5: The results of $2LiBH_4$-MgH_2 with 20 mol% $3TiCl_3{\cdot}AlCl_3$ after desorption: HRTEM image acquired from the position of purple agglomerates in Figure 4a, and the corresponding FFT, showing the existence of TiB_2 (and AlB_2); Figure S6: The results of $2LiBH_4$-MgH_2 with 20 mol% $3TiCl_3{\cdot}AlCl_3$ after desorption: (a) STEM-HAADF image showing the distribution of MgB_2 platelets; (b) electron diffraction patterns showing the crystallographic orientation of the corresponding MgB_2 platelets indicated in (a); Figure S7: Simulated superimposed diffraction patterns of MgB_2/Mg (a,b), and MgB_2/TiB_2 (c,d); Table S1: The interatomic misfit between $\langle 0002 \rangle_{MgB_2}$ and the possible matching directions of Mg nucleation center (%); Table S2: The interatomic misfit between $\langle 0002 \rangle_{MgB_2}$ and the possible matching directions of MB_2 (M = Ti or Al) nucleation center (%).

Author Contributions: Conceptualization, O.J., C.P. and A.P.; Data curation, O.J. and A.P.; Formal analysis, O.J., Y.S., X.H., X.M., D.V.S., T.T.L., S.W. and A.P.; Funding acquisition, C.P. and A.P.; Investigation, O.J., Y.S., X.H. and X.M.; Methodology, O.J., Y.S., X.H., X.M., D.V.S., S.W., C.K., C.P. and A.P.; Project administration, C.K., C.P. and A.P.; Resources, C.P. and A.P.; Software, O.J., Y.S., X.H., X.M., D.V.S., T.T.L. and S.W.; Supervision, D.V.S., C.P. and A.P.; Validation, O.J., X.H., X.M., D.V.S., T.T.L., S.W., C.K., C.P. and A.P.; Visualization, O.J., Y.S., X.H., D.V.S., S.W., C.K., C.P. and A.P.; Writing—original draft, O.J. and Y.S.; Writing—review & editing, O.J., Y.S., X.H., X.M., D.V.S., T.T.L., S.W., C.K., C.P. and A.P.. All authors have read and agreed to the published version of the manuscript.

Funding: This research was funded by Deutsche Forschungsgemeinschaft grant number PU 131/16-1 and PI 1488/2-1.

Institutional Review Board Statement: Not applicable.

Informed Consent Statement: Not applicable.

Data Availability Statement: The data that support the findings of this study are openly available in KITOpen under https://publikationen.bibliothek.kit.edu/1000140178 (accessed on 1 January 2022).

Acknowledgments: The authors would like to thank DFG (Deutsche Forschungsgemeinschaft) for funding this project (PU 131/16-1 and PI 1488/2-1) and KNMF (Karlsruhe Nano Micro Facility) for the experimental support. X.H. acknowledges the China Scholarship Council (CSC) for supporting her research at Karlsruhe Institute of Technology. We acknowledge support from the KIT-Publication Fund of the Karlsruhe Institute of Technology.

Conflicts of Interest: The authors declare no conflict of interest.

References

1. Milanese, C.; Jensen, T.; Hauback, B.; Pistidda, C.; Dornheim, M.; Yang, H.; Lombardo, L.; Zuettel, A.; Filinchuk, Y.; Ngene, P. Complex hydrides for energy storage. *Int. J. Hydrog. Energy* **2019**, *44*, 7860–7874. [CrossRef]
2. Chen, P.; Xiong, Z.; Luo, J.; Lin, J.; Tan, K.L. Interaction of hydrogen with metal nitrides and imides. *Nature* **2002**, *420*, 302–304. [CrossRef]
3. Barkhordarian, G.; Klassen, T.; Dornheim, M.; Bormann, R. Unexpected kinetic effect of MgB_2 in reactive hydride composites containing complex borohydrides. *J. Alloy. Compd.* **2007**, *440*, L18–L21. [CrossRef]
4. Vajo, J.J.; Salguero, T.T.; Gross, A.F.; Skeith, S.L.; Olson, G.L. Thermodynamic destabilization and reaction kinetics in light metal hydride systems. *J. Alloy. Compd.* **2007**, *446*, 409–414. [CrossRef]
5. Hauback, B.C. Task 22 of IEA HIA—Fundamental and Applied Hydrogen Storage Materials Development. In *18th World Hydrogen Energy Conference 2010-WHEC 2010*; Detlef Stolten, T.G., Ed.; Forschungszentrum Juelich GmbH: Essen, Germany, 2010.
6. Bösenberg, U.; Doppiu, S.; Mosegaard, L.; Barkhordarian, G.; Eigen, N.; Borgschulte, A.; Jensen, T.R.; Cerenius, Y.; Gutfleisch, O.; Klassen, T. Hydrogen sorption properties of MgH_2–$LiBH_4$ composites. *Acta Mater.* **2007**, *55*, 3951–3958. [CrossRef]
7. Mauron, P.; Buchter, F.; Friedrichs, O.; Remhof, A.; Bielmann, M.; Zwicky, C.N.; Züttel, A. Stability and reversibility of $LiBH_4$. *J. Phys. Chem. B* **2008**, *112*, 906–910. [CrossRef] [PubMed]
8. Orimo, S.-I.; Nakamori, Y.; Kitahara, G.; Miwa, K.; Ohba, N.; Towata, S.-I.; Züttel, A. Dehydriding and rehydriding reactions of $LiBH_4$. *J. Alloy. Compd.* **2005**, *404*, 427–430. [CrossRef]
9. Vajo, J.J.; Olson, G.L. Hydrogen storage in destabilized chemical systems. *Scr. Mater.* **2007**, *56*, 829–834. [CrossRef]
10. Vajo, J.J.; Skeith, S.L.; Mertens, F. Reversible storage of hydrogen in destabilized $LiBH_4$. *J. Phys. Chem. B* **2005**, *109*, 3719–3722. [CrossRef]
11. Bösenberg, U.; Kim, J.W.; Gosslar, D.; Eigen, N.; Jensen, T.R.; von Colbe, J.B.; Zhou, Y.; Dahms, M.; Kim, D.; Günther, R. Role of additives in $LiBH_4$–MgH_2 reactive hydride composites for sorption kinetics. *Acta Mater.* **2010**, *58*, 3381–3389. [CrossRef]
12. Bösenberg, U.; Ravnsbæk, D.B.; Hagemann, H.; D'Anna, V.; Minella, C.B.; Pistidda, C.; van Beek, W.; Jensen, T.R.; Bormann, R.d.; Dornheim, M. Pressure and temperature influence on the desorption pathway of the $LiBH_4 - MgH_2$ composite system. *J. Phys. Chem. C* **2010**, *114*, 15212–15217. [CrossRef]
13. Gross, A.F.; Vajo, J.J.; van Atta, S.L.; Olson, G.L. Enhanced hydrogen storage kinetics of $LiBH_4$ in nanoporous carbon scaffolds. *J. Phys. Chem. C* **2008**, *112*, 5651–5657. [CrossRef]
14. Gosalawit–Utke, R.; Thiangviriya, S.; Javadian, P.; Laipple, D.; Pistidda, C.; Bergemann, N.; Horstmann, C.; Jensen, T.R.; Klassen, T.; Dornheim, M. Effective nanoconfinement of $2LiBH_4$–MgH_2 via simply MgH_2 premilling for reversible hydrogen storages. *Int. J. Hydrog. Energy* **2014**, *39*, 15614–15626. [CrossRef]
15. Huang, X.; Xiao, X.; Shao, J.; Zhai, B.; Fan, X.; Cheng, C.; Li, S.; Ge, H.; Wang, Q.; Chen, L. Building robust architectures of carbon-wrapped transition metal nanoparticles for high catalytic enhancement of the $2LiBH_4$-MgH_2 system for hydrogen storage cycling performance. *Nanoscale* **2016**, *8*, 14898–14908. [CrossRef]
16. Deprez, E.; Justo, A.; Rojas, T.; López-Cartés, C.; Minella, C.B.; Bösenberg, U.; Dornheim, M.; Bormann, R.; Fernández, A. Microstructural study of the $LiBH_4$–MgH_2 reactive hydride composite with and without Ti-isopropoxide additive. *Acta Mater.* **2010**, *58*, 5683–5694. [CrossRef]
17. Fan, M.-Q.; Sun, L.-X.; Zhang, Y.; Xu, F.; Zhang, J.; Chu, H.-l. The catalytic effect of additive Nb2O5 on the reversible hydrogen storage performances of $LiBH_4$–MgH_2 composite. *Int. J. Hydrog. Energy* **2008**, *33*, 74–80. [CrossRef]
18. Le, T.-T.; Pistidda, C.; Puszkiel, J.n.; Riglos, M.a.V.C.; Karimi, F.; Skibsted, J.; GharibDoust, S.P.; Richter, B.; Emmler, T.; Milanese, C. Design of a nanometric AlTi additive for MgB_2-based reactive hydride composites with superior kinetic properties. *J. Phys. Chem. C* **2018**, *122*, 7642–7655. [CrossRef]
19. Kremer, J.R.; Mastronarde, D.N.; McIntosh, J.R. Computer visualization of three-dimensional image data using IMOD. *J. Struct. Biol.* **1996**, *116*, 71–76. [CrossRef]
20. Gilbert, P. Iterative methods for the three-dimensional reconstruction of an object from projections. *J. Theor. Biol.* **1972**, *36*, 105–117. [CrossRef]
21. Wold, S.; Esbensen, K.; Geladi, P. Principal component analysis. *Chemom. Intell. Lab. Syst.* **1987**, *2*, 37–52. [CrossRef]
22. Abdi, H.; Williams, L.J. Principal component analysis. *Wiley Interdiscip. Rev. Comput. Stat.* **2010**, *2*, 433–459. [CrossRef]
23. Lee, S. Crystal growth of MgB_2. *Phys. C Supercond.* **2003**, *385*, 31–41. [CrossRef]
24. Kong, X.; Wang, Y.; Li, H.; Duan, X.; Yu, R.; Li, S.; Li, F.; Jin, C. Electron energy-loss spectroscopy characterization of the boron p-like density of states in MgB_2. *Appl. Phys. Lett.* **2002**, *80*, 778–780. [CrossRef]

25. Deprez, E.; Munoz-Márquez, M.A.; Roldán, M.A.; Prestipino, C.; Palomares, F.J.; Minella, C.B.; Bosenberg, U.; Dornheim, M.; Bormann, R.; Fernández, A. Oxidation state and local structure of Ti-based additives in the reactive hydride composite $2LiBH_4$+ MgH_2. *J. Phys. Chem. C* **2010**, *114*, 3309–3317. [CrossRef]
26. Fan, X.; Xiao, X.; Chen, L.; Wang, X.; Li, S.; Ge, H.; Wang, Q. High catalytic efficiency of amorphous TiB_2 and NbB_2 nanoparticles for hydrogen storage using the $2LiBH_4$–MgH_2 system. *J. Mater. Chem. A* **2013**, *1*, 11368–11375. [CrossRef]
27. Zhang, M.-X.; Kelly, P. Edge-to-edge matching model for predicting orientation relationships and habit planes—the improvements. *Scr. Mater.* **2005**, *52*, 963–968. [CrossRef]
28. Zhang, M.-X.; Kelly, P. Edge-to-edge matching and its applications: Part II. Application to Mg–Al, Mg–Y and Mg–Mn alloys. *Acta Mater.* **2005**, *53*, 1085–1096. [CrossRef]
29. Zhang, M.-X.; Kelly, P.M.; Easton, M.A.; Taylor, J.A. Crystallographic study of grain refinement in aluminum alloys using the edge-to-edge matching model. *Acta Mater.* **2005**, *53*, 1427–1438. [CrossRef]
30. Kelly, P.; Zhang, M.-X. Edge-to-edge matching—The fundamentals. *Metall. Mater. Trans. A* **2006**, *37*, 833–839. [CrossRef]
31. Yang, J.; Wang, J.; Wu, Y.; Wang, L.; Zhang, H. Extended application of edge-to-edge matching model to HCP/HCP (α-Mg/$MgZn_2$) system in magnesium alloys. *Mater. Sci. Eng. A* **2007**, *460*, 296–300. [CrossRef]